AIMS Mathematics, 11(2): 5006–5028.
DOI: 10.3934/math.2026205
Received: 19 October 2025
Revised: 04 February 2026
Accepted: 06 February 2026
Published: 27 February 2026

https://www.aimspress.com/journal/Math

Research article

Thermal and solutal boundary layer of a third grade Ellis fluid over a vertical cylinder with cross-diffusion and reaction effects

Nadeem Abbas* and Wasfi Shatanawi

Department of Mathematics and Sciences, College of Sciences and Humanities, Prince Sultan University, Riyadh, 11586, Saudi Arabia

*** Correspondence:** Email: nabbas@psu.edu.sa.

Abstract: We investigated the boundary-layer flow, heat, and mass transfer characteristics of a third-grade Ellis fluid over a vertical stretching cylinder. The Ellis model was modified with third-grade fluid terms, properly representing the shear-dependent viscosity and higher-order nonlinear stress behaviors characteristic of fluids used for industrial purposes and polymers. Governing equations were derived to account for momentum, thermal, and solutal transport, while emphasizing the coupled influence of the Soret effect (mass flux due to thermal gradients) and the Dufour effect (heat flux induced by concentration gradients). Moreover, the species transport equation incorporated a first-order chemical reaction for modeling. Through the use of similarity transformations, the original nonlinear partial differential equations were converted into a set of coupled ordinary differential equations, which were then solved using numerical techniques. The impacts of various physical factors are presented in both tabular and graphical form. Velocity increased due to an increase in the Ellis fluid factor. The Ellis fluid parameter indicated that the fluid's effective viscosity decreased under shear. As a result, higher values of the Ellis fluid parameter reduce flow resistance, increasing the velocity profile throughout the surface.

Keywords: third-grade Ellis fluid; impacts of Soret and Dufour; vertical stretching cylinder; chemical reaction; numerical analysis
Mathematics Subject Classification: 35-XX, 20B40, 65-XX, 34-XX, 81T80

Nomenclature

k	Thermal conductivity	c_p	Heat capacity
k_T	Thermal diffusion ratio	D_s	Mass diffusivity
c_s	Concentration susceptibility	Ec	Eckert number
k_0	Chemical reaction	C	Concentration
T	Temperature	C_w	Wall concentration
T_w	Wall temperature	K	Curvature of cylinder
v	Kinematic viscosity	R	Material constant of Ellis fluid
(u, v)	Velocity components	ρ	Density
x	Axial direction	μ	Dynamic viscosity
r	Radial direction	τ_0	Material constant for Ellis fluid
F	Dimensionless velocity	α	Thermal diffusivity
β^*_3	Material constant for third-grade fluid	α^*_1	Material constant for third-grade fluid
α^*_2	Material constant for third-grade fluid	β_t	Coefficient of thermal expansion
g	Gravity	β_c	Coefficient of concentration expansion
C_∞	Ambient concentration	T_∞	Ambient temperature
β	Ellis fluid parameter	α_0	Material parameter of third-grade fluid
β_0	Material parameter of third-grade fluid	γ_0	Material parameter of third-grade fluid
Re	Reynold number	G_c	Concentration Grashoff factor
G_r	Thermal Grashoff factor	D_f	Dufour number
λ_0	Chemical reaction	Sc	Schmidt number
S_r	Soret number	Pr	Prandtl number
θ	Dimensionless temperature	ϕ	Dimensionless concentration

1. Introduction

The Ellis fluid model describes a non-Newtonian fluid that exhibits shear-thinning behavior at higher shear rates; at low shear stresses, it behaves like a viscous fluid. Such characteristics differentiate Ellis fluids from Newtonian fluids. When a fluid flows over a stretching cylinder, the combined effects of surface stretching and curvature greatly impact the boundary layer characteristics. The stretching of the cylinder surface induces an axial flow that enhances momentum transport, while the nonlinear rheology of Ellis fluids changes the velocity and stress distributions compared to Newtonian cases. These fluids have numerous applications, namely in polymer extrusion, wire coating, fiber manufacturing, and mass transfer processes, and present significance in enhancing industrial efficiency and exploring the rheological influence on boundary layer dynamics. The ground-breaking contributions of Matsuhisa and Bird [1] provided analytical and numerical solutions for the laminar flow of Ellis fluid. Li et al. [2] considered the motion of an Ellis fluid in fractal porous media. Kheyfets and Kieweg [3] studied the gravity-driven thin film of an Ellis fluid and its behavior. Ali et al. [4] formulated a mathematical model for an Ellis fluid subject to peristaltic pumping and electroosmotic effects within axisymmetric tubes comprising two fluid phases. Chemi -cal reactions in the peristaltic pumping of the Ellis fluid were studied by Abbasi et al. [5]. Metachronal wave impulsion in the two-layer system of the Ellis fluid was evaluated by Shaheen et al. [6]. Mishra [7] investigated a similar problem by analyzing radiative Ellis hybrid nanofluid flow over a stretching/shrinking cylinder embedded in a porous medium with slip conditions. They incorporated the combined effects of Joule heating, viscous dissipation, and magnetic fields and

found a significant role of electromagnetic forces and thermal effects in controlling microchannel flow. Abdal et al. [8] examined the influence of nanoparticle concentration on the heat and mass transfer characteristics of Ellis fluid flow across a stretching wall.

The study of non-Newtonian fluid flows is now a vital part of current fluid mechanics due to their wide use in polymer engineering, chemical processes, and medical systems. Among the different viscometric models, the third-grade fluid model has gained considerable attention because it is more realistic than both Newtonian and second-grade fluids in dealing with the behavior of complex fluids. Unlike Newtonian fluids, which follow a linear stress–strain relationship, third-grade fluids demonstrate nonlinear constitutive behavior characterized by additional material parameters. These parameters enable the model to capture essential features such as shear-thinning, shear-thickening, normal stress differences, and elastic recovery effects. Sahoo [9] focused on the Hiemenz flow and associated heat transfer properties in a third-grade fluid. Hayat et al. [10] analyzed axisymmetric magnetohydrodynamic flow and thermal transport for a third-grade fluid situated between two stretching sheets. Hayat et al. [11] explored axisymmetric MHD flow around a stretching cylinder, highlighting how geometry and magnetic field strength impact both velocity and temperature profiles. Akinshilo [12] discussed the steady motion and thermal exchange of a third-grade fluid moving through porous media with internal heat sources. Khan et al. [13] addressed non-Newtonian fluid transport over a porous surface undergoing stretching and shrinking, including thermal effects. Fatima et al. [14] examined electro-osmotic forces driving two-phase flow of a fourth-grade fluid in a channel with converging and diverging walls. Nadeem et al. [15] studied a magnetized generalized second-grade fluid flow in an oscillating rectangular duct, incorporating a time-fractional modeling approach. Their study emphasized the role of fractional derivatives in capturing memory effects and the complex flow responses that occur under magnetic fields. Xin et al. [16] examined the flow of third-grade fluids in porous media-saturated vertical microchannels, particularly in the presence of exothermic chemical reactions. Their numerical simulations provided useful information about heat transfer enhancement and reactive transport phenomena at a microscale. Abbas et al. [17] conducted a theoretical analysis of magnetohydrodynamic (MHD) Darcy–Forchheimer porous media. They focused on hybrid nanomaterial flow involving a third-grade fluid over an exponentially stretching sheet.

The Soret and Dufour effects are fundamental cross-diffusion phenomena observed in multicomponent fluid systems. The Soret effect, also known as thermal diffusion, refers to the mass flux induced by a temperature gradient. This phenomenon is particularly significant in micro- and nanoscale flows, chemical reactors, and geophysical processes. Conversely, the Dufour effect describes the energy flux caused by concentration gradients. Variations in species concentration result in additional heat transfer within the fluid. Accurate consideration of these effects is crucial for the design and optimization of industrial processes, such as chemical reactors, heat exchangers, and microfluidic devices. Kim et al. [18] analyzed convective instabilities in binary nanofluid and demonstrated that Soret and Dufour effects significantly impact absorption processes. Moorthy and Senthilvadivu [19] investigated the effects of variable viscosity on natural convection along a vertical surface embedded within a porous medium. Majeed et al. [20] analyzed the flow characteristics of a second-grade fluid around a stretching cylinder. Malik et al. [21] evaluated heat and mass transfer under mixed convection by an inclined cylinder surface. They used a non-Newtonian fluid model to analyze the impact of Joule heating in the stagnation region. Shojaei et al. [22] examined the coupled thermal and flow phenomena for a non-Newtonian second-grade fluid over a radiative stretching cylinder, paying particular attention to the roles of Soret and Dufour cross-diffusion processes. Their findings highlighted how the coupling of thermal and solutal diffusion can significantly alter the

temperature and concentration fields. Khan et al. [23] analyzed micropolar fluid flows over a nonlinear stretching cylinder. Their work demonstrated the sensitivity of velocity and thermal distributions to nonlinear stretching and micropolar parameters. Kumar et al. [24] conducted a thermal analysis using Williamson fluid flow over a permeable stretching cylinder. Basha [25] investigated a Casson fluid flow under the impact of magnetic fields and radiation, incorporating Soret and Dufour mechanisms through Cattaneo–Christov formulations for heat and mass transfer. Dharmaiah et al. [26] numerically evaluated the thermal effects of mucus fluid and detailed chemical reaction impacts. Thiyagarajan et al. [27] reported the impression of activation energy with a wavy cylinder. Thabet et al. [28] highlighted the impacts of the coupled stress of slip and viscous dissipation. Abd-Alla et al. [29] discussed the thermal variable properties under mixed convection impacts. Ali et al. [30] examined a Sutterby nanofluid motion past a Riga stretching sheet, highlighting the role of Soret and Dufour effects. Ahmed et al. [31] discussed the influence of these cross-diffusion processes on the flow of a third-grade fluid over a stretching cylinder.

Studying heat and mass transfer in non-Newtonian fluids is scientifically significant as they are widely used in different areas, from polymer processing to food engineering, chemical industries, and biomedical systems. Frequently, classical Newtonian models do not work properly with these fluids, meaning that advanced models must be used, such as the third-grade Ellis fluid model. This model considers both shear-dependent viscosity and nonlinear stress effects. Analyzing the flow over a vertical stretching cylinder is particularly pertinent to processes like fiber spinning, wire coating, extrusion, and glass manufacturing, where cylindrical geometries and stretching surfaces play a crucial role in ensuring product quality and efficiency. The transport phenomena in these scenarios are further complicated by cross-diffusion processes, including the Soret effect, which involves thermal gradients driving mass transfer, and the Dufour effect, where concentration gradients lead to additional heat flux. These effects hold considerable importance in multicomponent mixtures, geophysical systems, and high-temperature applications. The physical factors involved were analyzed here, and the proposed model was numerically solved. The results are presented in both tabular and graphical formats. These results will have applications in engineering and industry.

2. Materials and methods

We consider a steady, incompressible laminar boundary layer flow of a third-grade Ellis fluid caused by a vertical stretching cylinder. The configuration of the flow is presented in Figure 1.

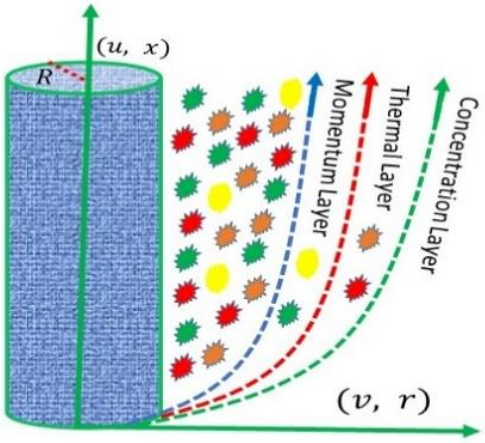

Figure 1. Flow pattern diagram.

The cylinder surface is stretched axially with a linearly increasing speed $u_w = \frac{U_0 x}{l}$ $(U_0 > 0)$, generating a thin viscous layer along the surface. Because the cylinder is vertical, the buoyancy effects arise due to temperature and concentration differences between the wall and the ambient fluid, which produce mixed convection. Cylindrical coordinates are defined as (x, r). The $x-$ along the cylinder axis and $r-$ normal to the surface are considered. The working fluid is modeled by a hybrid constitutive description: (i) Ellis shear-thinning viscosity for the first Rivlin–Ericksen contribution, and (ii) third-grade normal-stress/elastic nonlinearities for higher-order kinematics. The Soret and Dufour effects are considered. Buoyancy includes both thermal and solutal contributions using the Boussinesq approximation with expansion coefficients β_t and β_c. The wall temperature and concentration are represented as T_w and C_w; ambient temperature tends to T_∞, and concentration tends to C_∞. Apply the boundary layer approximation on the governing equation and reduce the system of partial differential equations defined as follows:

$$\frac{\partial u}{\partial x} + \frac{\partial v}{\partial r} + \frac{v}{r} = 0, \tag{1}$$

$$\begin{aligned}
&\rho\left(u\frac{\partial u}{\partial x} + v\frac{\partial v}{\partial r}\right) \\
&= \mu\frac{1}{r}\frac{\partial}{\partial r}\left(\frac{r}{1+\left[\frac{1}{\sqrt{2}\tau_0{}^2}\frac{\partial \mathrm{u}}{\partial r}\right]^{\alpha-1}}\frac{\partial \mathrm{u}}{\partial r}\right) + \beta^*{}_3\left(\left(\frac{\partial \mathrm{u}}{\partial r}\right)^3\frac{2}{r} + 6\frac{\partial^2 \mathrm{u}}{\partial r^2}\left(\frac{\partial \mathrm{u}}{\partial r}\right)^2\right) \\
&+ \alpha^*{}_1\left(\frac{u}{r}\frac{\partial^2 \mathrm{u}}{\partial \mathrm{r}\partial \mathrm{x}} + \frac{\partial^2 \mathrm{u}}{\partial r^2}\frac{v}{r} + \frac{3}{r}\frac{\partial \mathrm{u}}{\partial x}\frac{\partial \mathrm{u}}{\partial r} + \frac{1}{r}\frac{\partial \mathrm{v}}{\partial r}\frac{\partial \mathrm{u}}{\partial r} + 4\frac{\partial \mathrm{u}}{\partial r}\frac{\partial^2 \mathrm{u}}{\partial \mathrm{r}\partial \mathrm{x}} + u\frac{\partial^3 \mathrm{u}}{\partial \mathrm{r}^2\partial \mathrm{x}}\right. \\
&\left. + 2\frac{\partial^2 \mathrm{u}}{\partial \mathrm{r}^2}\frac{\partial \mathrm{v}}{\partial r} + v\frac{\partial^3 \mathrm{u}}{\partial \mathrm{r}^3} + 3\frac{\partial^2 \mathrm{u}}{\partial r^2}\frac{\partial \mathrm{u}}{\partial x} + \frac{\partial^2 \mathrm{v}}{\partial r^2}\frac{\partial \mathrm{u}}{\partial r}\right) \\
&+ \alpha^*{}_2\left(\frac{\partial \mathrm{v}}{\partial r}\frac{\partial \mathrm{u}}{\partial r}\frac{2}{r} + \frac{\partial \mathrm{v}}{\partial r}\frac{\partial \mathrm{u}}{\partial r}\frac{x}{r} + 2\frac{\partial \mathrm{v}}{\partial r}\frac{\partial^2 \mathrm{u}}{\partial r^2} + 2\frac{\partial^2 \mathrm{u}}{\partial r^2}\frac{\partial \mathrm{u}}{\partial x} + 4\frac{\partial^2 \mathrm{u}}{\partial \mathrm{r}\partial \mathrm{x}}\frac{\partial \mathrm{u}}{\partial r}\right) \\
&+ \rho g\beta_t(T - T_\infty) + \rho g\beta_c(C - C_\infty),
\end{aligned} \tag{2}$$

$$\begin{aligned}
&\left(u\frac{\partial T}{\partial x}+v\frac{\partial T}{\partial r}\right)\\
&=\frac{k}{\rho c_p}\left(\frac{\partial^2 \mathrm{T}}{\partial r^2}+\frac{1}{r}\frac{\partial \mathrm{T}}{\partial r}\right)+\frac{D_s k_T}{c_s c_p}\left(\frac{\partial^2 \mathrm{C}}{\partial r^2}+\frac{1}{r}\frac{\partial \mathrm{C}}{\partial r}\right)\\
&+\frac{\mu}{\rho c_p}\left(\frac{1}{1+\left[\frac{1}{\sqrt{2}{\tau_0}^2}\frac{\partial \mathrm{u}}{\partial r}\right]^{\alpha-1}}\frac{\partial \mathrm{u}}{\partial r}+2{\beta^*}_3\left(\frac{\partial \mathrm{u}}{\partial r}\right)^3\right.\\
&+{\alpha^*}_1\left(u\frac{\partial^2 \mathrm{u}}{\partial \mathrm{r}\partial \mathrm{x}}+v\frac{\partial^2 \mathrm{u}}{\partial r^2}+3\frac{\partial \mathrm{u}}{\partial x}\frac{\partial \mathrm{u}}{\partial r}+\frac{\partial \mathrm{v}}{\partial r}\frac{\partial \mathrm{u}}{\partial r}\right)\\
&\left.+{\alpha^*}_2\left(2\frac{\partial \mathrm{v}}{\partial r}\frac{\partial \mathrm{u}}{\partial r}+2\frac{\partial \mathrm{u}}{\partial x}\frac{\partial \mathrm{u}}{\partial r}\right)\right)\left(\frac{\partial \mathrm{u}}{\partial r}\right)
\end{aligned} \tag{3}$$

$$\left(u\frac{\partial C}{\partial x}+v\frac{\partial C}{\partial r}\right)=D_s\left(\frac{\partial^2 \mathrm{C}}{\partial r^2}+\frac{1}{r}\frac{\partial \mathrm{C}}{\partial r}\right)+\frac{D_s k_T}{T_\infty}\left(\frac{\partial^2 \mathrm{T}}{\partial r^2}+\frac{1}{r}\frac{\partial \mathrm{T}}{\partial r}\right)-k_0(C-C_\infty). \tag{4}$$

Here, C_∞ and T_∞ are the ambient concentration and temperature, and u and v are the mechanisms of velocity in the direction of $(x,\ r)$. The fluid velocity tends to zero in the axial and radial directions, implying that flow becomes negligible as it approaches infinity (far away from the surface). The fluid motion asymptotically approaches a large distance from the origin. Boundary conditions are essential for cracking the governing equations related to fluid flow, mass transport, and heat transfer in an Ellis third-grade fluid system. The boundary conditions are as follows:

$$\begin{aligned}
&u=\tfrac{U_0 x}{l}, v=0, T=T_w, C=C_w, \text{as } r=A,\\
&u=0, \tfrac{\partial \mathrm{u}}{\partial r}=0, T=T_\infty, C=C_\infty \text{as } r=\infty.
\end{aligned} \tag{5}$$

The necessary transformations to simplify the differential equations are stated as follows:

$$\begin{aligned}
&\xi=\left(\frac{r^2-A^2}{2A}\right)\sqrt{\frac{U_0}{l\upsilon}},\quad u=\frac{U_0 x}{l}F_\xi,\quad v=-\frac{A}{r}\sqrt{\frac{U_0\upsilon}{l}}F(\xi),\\
&\theta(\xi)=\frac{T-T_w}{T_w-T_\infty},\quad \phi(\xi)=\frac{C-C_w}{C_w-C_\infty}.
\end{aligned} \tag{6}$$

The transformations applied to the above equation and system become dimensionless, defined as follows:

$$\frac{(1+2\xi K)\left(1+(2-R)\left(\beta F_{\xi\xi}\right)^{R-1}\right)F_{\xi\xi\xi}+K\left(1+(2-R)\left(\beta F_{\xi\xi}\right)^{R-1}\right)F_{\xi\xi}}{\left[1+\left(\beta F_{\xi\xi}\right)^{R-1}\right]^{2}}-F_{\xi}F_{\xi}+FF_{\xi\xi}$$
$$+\alpha_0\left((1+2\xi K)\{3F_{\xi\xi}F_{\xi\xi}-FF_{\xi\xi\xi\xi}+2F_{\xi}F_{\xi\xi}\}-K\left(2FF_{\xi\xi\xi}-6F_{\xi}F_{\xi\xi}\right)\right)$$
$$+\beta_0\left(2F_{\xi\xi}F_{\xi\xi}(1+2\xi K)+K\left(2FF_{\xi\xi\xi}+2F_{\xi}F_{\xi\xi}\right)\right) \tag{7}$$
$$+Re\gamma_0\left(6(1+2\xi K)(1+2\xi K)F_{\xi\xi}F_{\xi\xi\xi}F_{\xi\xi}+8KF_{\xi\xi}F_{\xi\xi}F_{\xi\xi}(1+2\xi K)\right)$$
$$+G_r\theta+G_c\phi=0,$$

$$\frac{1}{Pr}\{(1+2\xi K)\theta_{\xi\xi}+2K\theta_{\xi}\}+F\theta_{\xi}+D_f\{(1+2\xi K)\phi_{\xi\xi}+2K\phi_{\xi}\}$$
$$+Ec(1+2\xi K)\left(\frac{1}{1+\left(\beta F_{\xi\xi}\right)^{R-1}}F_{\xi\xi}+2(1+2\xi K)\gamma_0F_{\xi\xi}F_{\xi\xi}F_{\xi\xi}\right. \tag{8}$$
$$\left.+\alpha_0\left(3F_{\xi}F_{\xi\xi}-FF_{\xi\xi\xi}+(1+2\xi K)KFF_{\xi\xi}\right)+\beta_02K(1+2\xi K)F_{\xi\xi}F\right)=0,$$

$$\{(1+2\xi K)\phi_{\xi\xi}+2K\phi_{\xi}\}+ScF\phi_{\xi}+ScS_r\{(1+2\xi K)\theta_{\xi\xi}+2K\theta_{\xi}\}-\lambda_0Sc\phi=0. \tag{9}$$

The simplified boundary conditions are as follows:

$$F=0,\quad F_{\xi}=1,\ \theta=1,\ \phi=1,\quad \text{as } \xi\to 0,$$
$$F_{\xi}=0,\ F_{\xi\xi}=0,\ \theta=0,\ \phi=0,\quad \text{as } \xi\to\infty. \tag{10}$$

The parameters are defined as follows:

β	Ellis fluid parameter	Gc	Concentration Grashoff factor
$\alpha_0,\beta_0,\gamma_0$	Material parameter of third-grade fluid	R	Material constant of Ellis fluid
S_r	Soret number	λ_0	Chemical reaction
Sc	Schmidt number	Pr	Prandtl number
Gr	Thermal Grashoff factor	D_f	Dufour number

The impression of Nusselt, skin friction, and Sherwood numbers are as follows:

$$Nu_x=\frac{xq_r}{k(T_w-T_\infty)},Sh_x=\frac{xh_w}{D_B(C_w-C_\infty)},\qquad C_f=\frac{\tau_w}{\rho{u_w}^2}. \tag{11}$$

Namely, $q_r=-k\left(\frac{\partial \mathrm{T}}{\partial r}\right)_{r=A},\tau_w=\left(\frac{\mu}{1+\left[\frac{1}{\sqrt{2}{\tau_0}^2}\frac{\partial \mathrm{u}}{\partial r}\right]^{\alpha-1}}\frac{\partial \mathrm{u}}{\partial r}+2{\beta^*}_3\left(\frac{\partial \mathrm{u}}{\partial r}\right)^3+{\alpha^*}_1\left(u\frac{\partial^2 \mathrm{u}}{\partial \mathrm{r}\partial \mathrm{x}}+v\frac{\partial^2 \mathrm{u}}{\partial r^2}+\right.\right.$

$\left.\left.3\frac{\partial \mathrm{u}}{\partial x}\frac{\partial \mathrm{u}}{\partial r}+\frac{\partial \mathrm{v}}{\partial r}\frac{\partial \mathrm{u}}{\partial r}\right)+{\alpha^*}_2\left(2\frac{\partial \mathrm{v}}{\partial r}\frac{\partial \mathrm{u}}{\partial r}+2\frac{\partial \mathrm{u}}{\partial x}\frac{\partial \mathrm{u}}{\partial r}\right)\right)_{r=A}$, and $h_w=-D_B\left(\frac{\partial \mathrm{C}}{\partial r}\right)_{r=A}$. Using the transformation on the above Eq (11), we obtain the following:

$$C_f Re^{1/2} = \left(\frac{F_{\xi\xi}}{1 + \left(\beta F_{\xi\xi}\right)^{1-R}} + 3\alpha_0 F_{\xi\xi} + 2Re\ \ \gamma_0 \left(F_{\xi\xi}\right)^3 \right)_{\xi=0}, Nu_x Re^{-1/2} = -\theta_{\xi\,\xi=0}, \quad Sh_x Re^{-\frac{1}{2}} = -\phi_{\xi\,\xi=0}. \tag{12}$$

3. Methodology scheme

The BVP4C solver from MATLAB is a robust numerical method designed to handle boundary value problems involving nonlinear ordinary differential equations (ODEs). It operates by transforming higher-order nonlinear equations into an equivalent system of first-order ODEs. The solver applies a collocation technique, which enhances both accuracy and stability in the numerical solution. Furthermore, BVP4C incorporates adaptive mesh refinement, automatically adjusting the distribution of grid points to focus on regions where the solution changes rapidly. The numerical procedure can be summarized as follows:

- The higher-order nonlinear ODE is rewritten as an equivalent system of first-order equations.
- The solution is approximated using cubic collocation (the interval is divided into mesh points, and the solution is represented by piecewise polynomials).
- The ODE and boundary conditions are enforced at selected collocation points and generate a system of nonlinear algebraic equations.
- The bvp4c solves the nonlinear algebraic system using a Newton iteration to effectively handle nonlinearity.
- The solver computes the Jacobian matrix required for Newton's method.
- The bvp4c checks the error across the mesh and automatically refines the mesh.
- The iterative process reduces the residuals of the ODE and boundary conditions until they meet the tolerance.
- The algorithm is designed to handle moderate stiffness and certain types of singular solutions common in nonlinear BVPs.
- The convergence depends heavily on providing a reasonable initial guess for the solution over the domain.
- The final solution is given as a continuous function that is evaluated at a given interval.

The mathematical expression is as follows:

$$X(1) = F(\xi);\ \ X(2) = F_\xi;\ \ F_{\xi\xi} = X(3);\ \ F_{\xi\xi\xi} = X(4);\ \ F_{\xi\xi\xi\xi} = XX1;$$
$$X(5) = \ \theta(\xi);\ \ X(6) = \theta_\xi;\ \ \theta_{\xi\xi} = XX2;\ \ \phi(\xi) = X(7);\quad X(8) = \phi_\xi;\quad \phi_{\xi\xi} = XX3; \tag{13}$$

$$
\begin{aligned}
&XX1\\
&= \frac{1}{\alpha_0 X(1)(1+2\xi K)}\Bigg(\frac{(1+2\xi K)\left(1+(2-R)\left(\beta X(3)\right)^{R-1}\right)X(4)+K\left(1+(2-R)\left(\beta X(3)\right)^{R-1}\right)X(3)}{\left[\left(1+\beta X(3)\right)^{R-1}\right]^2}\\
&-X(2)X(2)+X(1)X(3)\\
&+\alpha_0\left((1+2\xi K)\{3X(3)X(3)+2X(2)X(3)\}-K\left(2X(1)X(4)-6X(2)X(3)\right)\right)\\
&+\beta_0\left(2X(3)X(3)(1+2\xi K)+K\left(2X(1)X(4)+2X(2)X(3)\right)\right)\\
&+Re\gamma_0\left(6(1+2\xi K)(1+2\xi K)X(4)X(3)X(3)+8KX(3)X(3)X(3)(1+2\xi K)\right)+G_rX(5)+G_cX(7)\Bigg);
\end{aligned}
\tag{14}
$$

$$
\begin{aligned}
XX2 = \frac{-Pr}{(1+2\xi K)}\Bigg(&X(6)X(1)+D_f\{(1+2\xi K)XX3+2KX(8)\}\\
&+Ec(1+2\xi K)\left(\frac{1}{1+(\beta X(3))^{R-1}}X(3)+2(1+2\xi K)\gamma_0X(3)X(3)X(3)\right.\\
&+\alpha_0(3X(2)X(3)-X(1)X(4)+(1+2\xi K)KX(3)X(1))\\
&\left.+\beta_0 2K(1+2\xi K)X(1)X(3)\right)\Bigg)-2KX(6);
\end{aligned}
\tag{15}
$$

$$
XX3 = \frac{-1}{(1+2\xi K)}\left(+ScX(1)X(8)+ScS_r\{(1+2\xi K)XX2+2KX(6)\}-\lambda_0ScX(7)\right)-2KX(8).
\tag{16}
$$

The boundary condition at surface is:

$$
\begin{gathered}
X_{2(0)}-1;\ \ X_{1(0)};\quad X_{3(\infty)};\ \ X_{2(\infty)};\quad X_{5(0)}-1;\ \ X_{5(\infty)};\\
X_{7(0)}-1;\qquad X_{7(\infty)}.
\end{gathered}
\tag{17}
$$

This system of equations was numerically solved using MATLAB's bvp4c solver, with the tolerance parameter specified as e^{-6}. The boundary residuals, denoted as $\tilde{R}_{Velocity}(\widetilde{u_1},\widetilde{u_2},\widetilde{u_3})$, $\tilde{R}_{Concentration}(\widetilde{u_1},\widetilde{u_2},\widetilde{u_3})$, $\tilde{R}_{Temperture}(\widetilde{u_1},\widetilde{u_2},\widetilde{u_3})$, were used to assess the accuracy of the solution. When these residuals fall below the predefined tolerance threshold of 10^{-6}, the difference between the computed results and the expected results is small, thus confirming the solution convergence. The residuals characterize the deviations of the numerical values obtained from the expected boundary conditions, as follows:

$$
\tilde{R}_{Velocity}(\widetilde{u_1},\widetilde{u_2},\widetilde{u_3}) = |\times_2(\infty)-\widehat{\times_2}(\infty)|,
$$

$$
\tilde{R}_{Temperture}(\widetilde{u_1},\widetilde{u_2},\widetilde{u_3}) = \left|X_5(\infty)-\widehat{X_5}(\infty)\right|,
$$

$$
\tilde{R}_{Concentration}(\widetilde{u_1},\widetilde{u_2},\widetilde{u_3}) = |\times_7(\infty)-\widehat{\times_7}(\infty)|.
$$

The computational process provides an exact determination of the boundary values. Newton's method shows effective convergence through the gradual improvement of the first guesses to the required degree of precision.

4. Results and discussion

The governing equations of the current model were solved numerically. The outcomes are provided in graphical and tabular forms for various physical parameters. Figures 2–4 present the effects of the material parameters of the Ellis fluid (R) and third-grade fluid (α_o, β_o) on velocity.

Variations in Ellis fluid velocity are presented in Figure 2. The velocity increases with an increase in the Ellis fluid parameter. The Ellis fluid parameter indicates how much the fluid deviates from Newtonian behavior, which typically leads to enhanced shear-thinning as the parameter increases. This implies that the effective viscosity of the fluid decreases under shear. As a result, higher values of the Ellis fluid parameter reduce flow resistance, which increases the velocity profile along the surface.

The variation of α_o with velocity is presented in Figure 3. Velocity increases due to increasing α_o. Similarly, the variation of β_o with velocity is presented in Figure 4, where velocity also increases with β_o. Physically, the third-grade fluid parameters represent nonlinear elastic and viscous effects. As their values increase, the nonlinear shear-thinning behavior reduces resistance to motion, allowing fluid layers to slide more easily. This enhances momentum transfer and increases the velocity profile near the stretching surface.

The influence of $\mathrm{D_f}$ on temperature is presented in Figure 5. The fluid temperature increases with increasing values of $\mathrm{D_f}$. Physically, the Dufour effect refers to heat flow generated by a concentration gradient in the fluid. As the Dufour parameter increases, more energy is transferred from regions of high concentration to regions of low concentration, resulting in an elevated temperature profile.

The influence of S_r on fluid temperature is shown in Figure 6. The temperature profile decreases with increasing values of S_r. Physically, the Soret effect represents mass diffusion induced by a temperature gradient. When the Soret parameter increases, stronger species diffusion absorbs part of the thermal energy for mass transport, reducing heat retention in the fluid. Consequently, the thermal field decreases, causing the temperature profile to decline.

The influence of S_r on fluid concentration is shown in Figure 7. Higher values of S_r enhance the fluid concentration. The variation of $\mathrm{D_f}$ with concentration is shown in Figure 8, where the opposite behavior is observed. The Dufour effect causes heat to flow due to the concentration gradient. As the Dufour parameter increases, the enhanced heat transfer promotes thermal diffusion, which reduces concentration differences. As a result, the concentration profile decreases because increased heat flux promotes mixing and reduces concentration gradients more rapidly. Increasing the Dufour effect causes a physical decline in the concentration at the stretching surface.

The variation of λ_0 with concentration is given in Figure 9. An inverse relationship is observed between concentration and λ_0. Physically, as the chemical reaction parameter increases, the rate of reactant consumption increases. The concentration profile decreases with stronger chemical reaction effects.

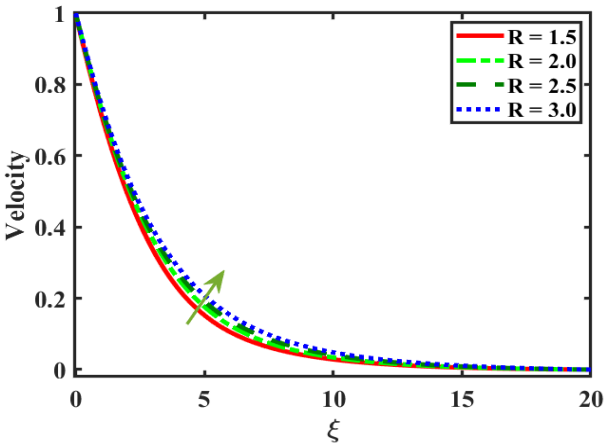

Figure 2. Behavior of R with velocity.

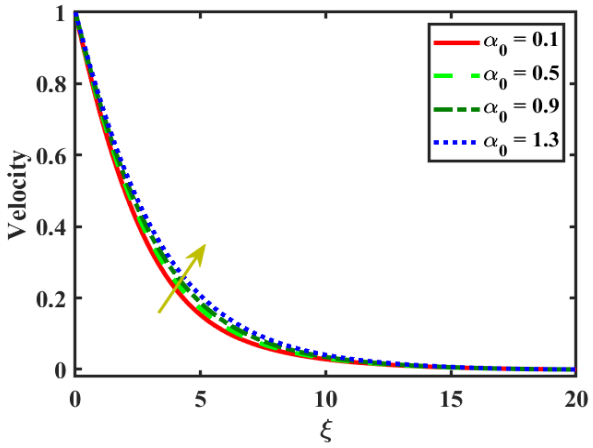

Figure 3. Behavior of α_o with velocity.

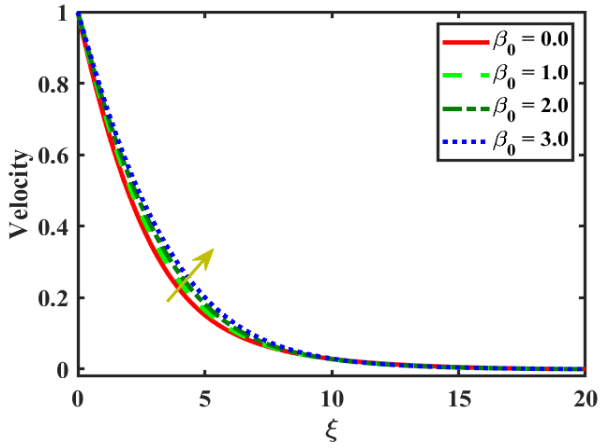

Figure 4. Behavior of β_o with velocity.

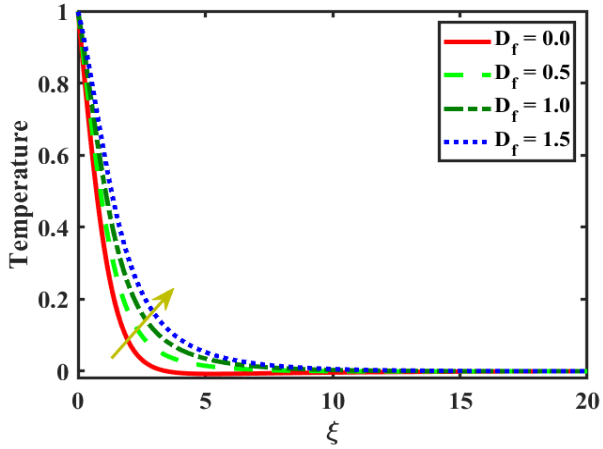

Figure 5. Behavior of $\mathrm{D_f}$ with temperature.

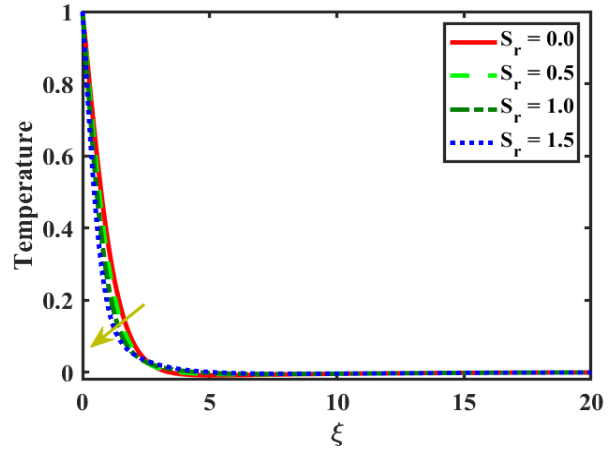

Figure 6. Behavior of S_r with temperature.

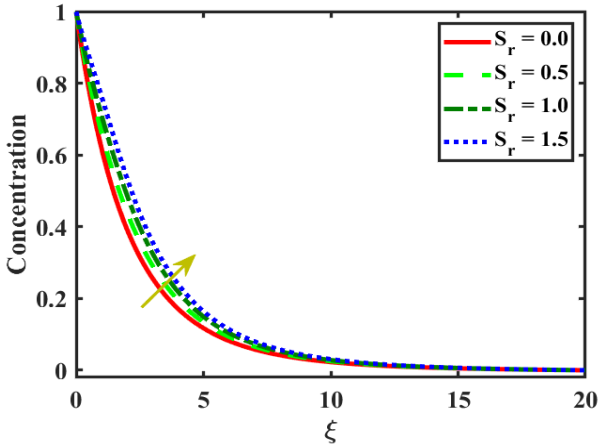

Figure 7. Behavior of S_r with concentration.

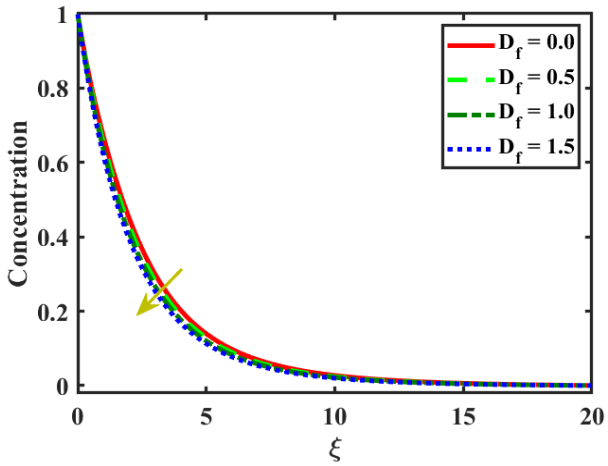

Figure 8. Behavior of D_{f} with concentration.

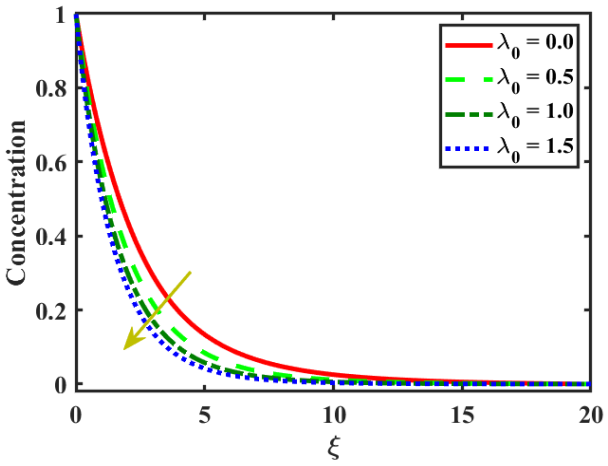

Figure 9. Behavior of λ_0 with concentration.

The Sherwood number ($Sh_x Re^{-\frac{1}{2}}$), skin friction ($C_f Re^{1/2}$), and Nusselt number ($Nu_x Re^{-1/2}$) represent the surface friction, mass transfer rate, and heat transfer rate, respectively. Their values fluctuate with changes in the physical parameters listed in Table 1.

An increase in the Dufour number ($\mathrm{D_f}$) increases the Sherwood number ($Sh_x Re^{-\frac{1}{2}}$) but decreases the Nusselt number ($Nu_x Re^{-1/2}$) and skin friction coefficient ($C_f Re^{1/2}$). A higher Dufour number indicates stronger energy transport from regions of high concentration to low concentration, which intensifies the coupling between heat and mass fields. This coupling enhances the concentration gradient at the wall, thereby increasing mass transfer rate. The thickening of the thermal layer reduces the wall temperature gradient, leading to a decrease in the Nusselt number. The reduced wall velocity gradient lowers the wall shear stress, causing a decline in skin friction.

As the Soret number (S_{r}) increases, the Sherwood number ($Sh_x Re^{-\frac{1}{2}}$) and skin friction ($C_f Re^{1/2}$) decrease, whereas Nusselt number increases ($Nu_x Re^{-1/2}$). A higher Soret number weakens the wall concentration gradient, reducing the dimensionless mass transfer rate and decreasing the Sherwood number. The reduced wall velocity gradient lowers wall shear stress, resulting in decreased skin friction. A steeper wall temperature gradient enhances the dimensionless heat transfer rate, leading to an increase in the Nusselt number.

The third-grade fluid parameter (γ_0) characterizes the non-Newtonian behavior of the fluid. Increasing this parameter enhances the Nusselt number, Sherwood number, and skin friction. Skin friction and Sherwood number also increase, while the Nusselt number declines, with an increase in (λ_0). A stronger wall concentration gradient enhanced the dimensionless mass transfer rate, and the Sherwood number increases with the chemical reaction parameter. A weaker wall temperature gradient reduces the dimensionless heat transfer rate. The Nusselt number decreases with a stronger chemical reaction.

An increase in the concentration Grashoff number (Gc) reduces skin friction while increasing both Nusselt and Sherwood numbers. Enhanced buoyancy improves convective transport, thinning the thermal and concentration boundary layers at the surface. Thinner boundary layers produce steeper temperature and concentration gradients at the wall. A reduced wall velocity gradient lowers the wall shear stress, leading to decreased skin friction. Thinner boundary layers enhance temperature and concentration gradients at the wall, increasing both Nusselt and Sherwood numbers.

Table 1. Numerical analysis of Sherwood number and Nusselt number for various physical factors.

D_f	S_r	γ_0	λ_0	Gc	Gr	Pr	R	Sc	Ec	$Sh_x Re^{-1/2}$	$Nu_x Re^{-1/2}$	$C_f Re^{1/2}$
0.0	0.5	0.3	0.5	0.4	0.5	2.5	2.5	0.2	0.1	0.42157045325	0.990373349490	1.65964500204
0.5	-	-	-	-	-	-	-	-	-	0.43196512721	0.823301827670	1.57764039276
1.0	-	-	-	-	-	-	-	-	-	0.44211401672	0.660563751032	1.50109421958
1.5	-	-	-	-	-	-	-	-	-	0.45215883694	0.501791370033	1.42972169414
0.5	0.0	-	-	-	-	-	-	-	-	0.49139544442	0.775741989082	1.60547164685
-	0.5	-	-	-	-	-	-	-	-	0.43196512721	0.823301827669	1.57764039276
-	1.0	-	-	-	-	-	-	-	-	0.36235509497	0.878893668377	1.55035180737
-	1.5	-	-	-	-	-	-	-	-	0.27945824941	0.945248174599	1.52299036125
-	0.5	0.0	-	-	-	-	-	-	-	0.424227925190	0.799970808189	0.75370090949
-	-	0.3	-	-	-	-	-	-	-	0.431965127207	0.823301827669	1.57764039276
-	-	0.6	-	-	-	-	-	-	-	0.435141065421	0.832441216276	2.01718354395
-	-	0.9				-	-	-	-	0.437221236358	0.838543838671	2.33866696871
-	-	0.3	0.0	-	-	-	-	-	-	0.266943636078	0.910563452843	1.44626496039
-	-	-	0.5	-	-	-	-	-	-	0.431965127207	0.823301827669	1.57764039276
-	-	-	1.0	-	-	-	-	-	-	0.547431277086	0.759752261746	1.64316556159
-	-	-	1.5	-	-	-	-	-	-	0.641571057604	0.706438103630	1.68515276482
-	-	-	0.5	0.0	-	-	-	-	-	0.428111802838	0.811663719204	2.12722583608
-	-	-	-	0.2	-	-	-	-	-	0.430086731610	0.817718984699	1.84685423927
-	-	-	-	0.4	-	-	-	-	-	0.431965127207	0.823301827669	1.57764039276
-	-	-	-	0.6	-	-	-	-	-	0.433710275892	0.8284872251322	1.32003734697
-	-	-	-	0.4	0.0	-	-	-	-	0.431372992178	0.8216548282050	1.86967890842
-	-	-	-	-	0.5	-	-	-	-	0.431965127207	0.8233018276692	1.57764039276
-	-	-	-	-	1.0	-	-	-	-	0.432553007078	0.825250962796	1.29217429874
-	-	-	-	-	1.5	-	-	-	-	0.433160589093	0.827450557304	1.01270948377
-	-	-	-	-	0.5	1.5	-	-	-	0.431965127207	0.823301827669	1.57764039276
-	-	-	-	-	-	2.0	-	-	-	0.422752570164	0.939936463820	1.59114439281
-	-	-	-	-	-	2.5	-	-	-	0.414300425560	1.042482736339	1.60086648720
-	-	-	-	-	-	3.0	-	-	-	0.406456057868	1.134956658607	1.60904135516
-	-	-	-	-	-	1.5	1.5	-	-	0.431965127207	0.823301827669	1.57764039276
-	-	-	-	-	-	-	2.0	-	-	0.432921102661	0.835003738626	1.51131816421
-	-	-	-	-	-	-	2.5	-	-	0.433601188792	0.833302282395	1.44229523096
-	-	-	-	-	-	-	3.0	-	-	0.434604122188	0.835835180220	1.38143471845
-	-	-	-	-	-	-	1.5	0.0	-	0.174913416613	0.94996296301	1.18908455410
-	-	-	-	-	-	-	-	0.2	-	0.431965127207	0.823301827669	1.57764039276
-	-	-	-	-	-	-	-	0.4	-	0.585235623971	0.762549777500	1.69596437925
-	-	-	-	-	-	-	-	0.6	-	0.716222968732	0.707282926554	1.75308823119
-	-	-	-	-	-	-	-	0.2	0.0	0.440595560346	0.6723544609087	1.478545609498
-	-	-	-	-	-	-	-	-	0.1	0.431965127207	0.8233018276692	1.577640392763
-	-	-	-	-	-	-	-	-	0.2	0.423053127552	0.9746257572922	1.668931173743
-	-	-	-	-	-	-	-	-	0.3	0.414155852647	1.126639505919	1.759706727695

As the Prandtl number (Pr) increases, the Sherwood number decreases, while the Nusselt number and skin friction increase. An increase in the Ellis fluid material parameter (R) decreases

skin friction but increases the Nusselt and Sherwood numbers. A higher Ellis parameter reduces effective viscosity near the wall under high shear rates, lowering wall shear stress and reducing skin friction. The shear-thinning behavior compresses the momentum boundary layer and also reduces the thermal and concentration boundary layers. This steepens the temperature and concentration gradients at the wall and enhances heat and mass transfer rates. An increase in the Schmidt number (Sc) decreases the Nusselt number but increases the Sherwood number and skin friction. Higher Sc numbers reduce mass diffusivity, thinning the concentration boundary layer while relatively thickening the thermal boundary layer, which lowers the heat transfer rate. The compressed concentration boundary layer steepens the wall concentration gradient, enhancing mass transfer. Reduced species diffusion strengthens near-wall velocity gradients, increasing skin friction. An increase in Ec decreases the Sherwood number but increases skin friction and Nusselt number.

Table 2 presents a comparison of the current work with previously published literature for different values of K, while other parameters remain fixed. The comparison shows good agreement with existing works.

Table 2. Comparison with literature for different values of K, while other parameters remain fixed.

K	Present results	Remash et al. [33]	Battacharya [32]
0.1	2.100346	2.100332	2.1003187
0.2	2.058867	2.058843	2.0588875
0.3	2.008854	2.008887	2.0088406

5. Response surface methodology (RSM)

Response surface methodology (RSM) is used to analyze the relationship between input factors and output responses in order to formulate the perfect correlation. This section shows the RSM for the Nusselt number as the output response and λ_0, S_r, and D_f as input factors, together with analysis of variance (ANOVA) and sensitivity results. The general relationship between output responses Nu and input parameters A, B, and C is defined as follows:

$$Nu = \Gamma_0 + \Gamma_1 A + \Gamma_2 B + \Gamma_3 C + \Gamma_4 AB + \Gamma_5 AC + \Gamma_6 BC + \Gamma_7 A^2 + \Gamma_8 B^2 + \Gamma_9 C^2, \tag{18}$$

where Γ_i, i = 0, 1,...,9 are the unknown constants, named regression coefficients. These regression coefficients will be determined by response surface methodology (RSM). The levels of parameters λ_0, S_r, and D_f at low (-1), medium (0), and high (+1) relevant positions are shown in Table 3.

Table 3. Symbolic representation of input factors with specific levels and values.

Parameters	Symbol	Levels		
		-1 (low)	0 (medium)	1 (high)
λ_0	A	0.5	1.0	1.5
S_r	B	0.5	1.0	1.5
D_f	C	0.3	0.6	0.9

For the RSM to run successfully, 20 runs and 19 degrees of freedom are required, as shown in Table 4.

Table 4. Experiment design with coded and actual estimations of parameters.

Experiment number	Coded values			Real values			Responses
	A	B	C	λ_0	S_r	D_f	Nusselt number
1	-1	-1	-1	0.5	0.5	0.3	0.8895791357
2	1	-1	-1	1.5	0.5	0.3	0.8176096714
3	-1	1	-1	0.5	1.5	0.3	1.0307595670
4	1	1	-1	1.5	1.5	0.3	0.9349373135
5	-1	-1	1	0.5	0.5	0.9	0.6927837475
6	1	-1	1	1.5	0.5	0.9	0.4881409047
7	-1	1	1	0.5	1.5	0.9	0.7790177553
8	1	1	1	1.5	1.5	0.9	0.5126318550
9	-1	0	0	0.5	1.0	0.6	0.8418190301
10	1	0	0	1.5	1.0	0.6	0.6829295454
11	0	-1	0	1.0	0.5	0.6	0.7148754369
12	0	1	0	1.0	1.5	0.6	0.8029608725
13	0	0	-1	1.0	1.0	0.3	0.9087479576
14	0	0	1	1.0	1.0	0.9	0.6056572548
15	0	0	0	1.0	1.0	0.6	0.7552705428
16	0	0	0	1.0	1.0	0.6	0.7552705428
17	0	0	0	1.0	1.0	0.6	0.7552705428
18	0	0	0	1.0	1.0	0.6	0.7552705428
19	0	0	0	1.0	1.0	0.6	0.7552705428
20	0	0	0	1.0	1.0	0.6	0.7552705428

Analysis of variance (ANOVA) is crucial to determine the significance of the correlations between input parameters. The regression coefficients given in Eq (18) were calculated using the MINITAB software. Tables 5 and 6 show all statistical estimations using ANOVA.

Equation (18) can be evaluated based on its P-value, which is useful for validating regression models. From a statically perspective, P-values smaller than 0.05 indicate significance, whereas P-values greater than or equal to 0.05 indicate statistical insignificance. It is observed that the constant terms, A and C are not significant based on the corresponding P-values, reported in Table 6. Therefore, Equation (18) takes the following form:

$$Nu = 0.75524 - 0.07977\ A + 0.04573\ B - 0.15034\ C + 0.00719\ A^2 + 0.00373\ B^2 + 0.00202\ C^2 - 0.01070\ AB - 0.03790\ AC - 0.01847\ BC. \tag{19}$$

The present model demonstrates a strong goodness of fit, supported by the coefficient of determination for Nu being 99.94%, as shown in Table 6, indicating high model accuracy.

Table 5. ANOVA for the Nusselt number.

Source	DF	Adj SS	Adj MS	F-value	P-value
Model	9	0.326351	0.036261	1903.36	0.000
Linear	3	0.310570	0.103523	5433.96	0.000
A	1	0.063634	0.063634	3340.17	0.000
B	1	0.020914	0.020914	1097.78	0.000
C	1	0.226022	0.226022	11863.93	0.000
Square	3	0.000641	0.000214	11.22	0.002
A ×A	1	0.000142	0.000142	7.46	0.021
B ×B	1	0.000038	0.000038	2.01	0.187
C ×C	1	0.000011	0.000011	0.59	0.462
2-way interaction	3	0.015140	0.005047	264.90	0.000
A ×B	1	0.000916	0.000916	48.07	0.000
A ×C	1	0.011494	0.011494	603.33	0.000
B ×C	1	0.002730	0.002730	143.30	0.000
Error	10	0.000191	0.000019		
Lack-of-fit	5	0.000191	0.000038	*	*
Pure error	5	0.000000	0.000000		
Total	19	0.326541			

Table 6. Regression coefficients for the Nusselt number (Nu).

Term	Coef	SE Coef	T-value	P-value	VIF
Constant	0.75524	0.00150	503.32	0.000	Yes
A	-0.07977	0.00138	-57.79	0.000	Yes
B	0.04573	0.00138	33.13	0.000	Yes
C	-0.15034	0.00138	-108.92	0.000	Yes
A ×A	0.00719	0.00263	2.73	0.021	Yes
B ×B	0.00373	0.00263	1.42	0.187	No
C ×C	0.00202	0.00263	0.77	0.462	No
A ×B	-0.01070	0.00154	-6.93	0.000	Yes
A ×C	-0.03790	0.00154	-24.56	0.000	Yes
B ×C	-0.01847	0.00154	-11.97	0.000	Yes
	$R^2 = 99.94\%$		Adj $R^2 = 99.89\%$		

Different error graphs are also shown in Figures 10(a)–(d) to validate the authenticity of current analysis. The assumptions of normality, independence, and randomness for the analysis of variance (ANOVA) are confirmed by residual plots.

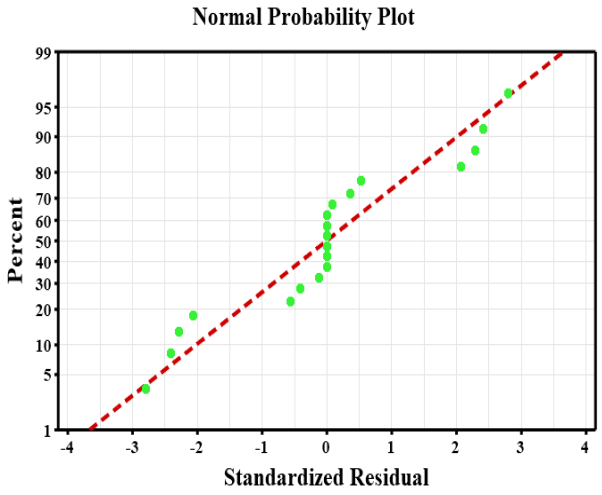

(a) Normal probability plot

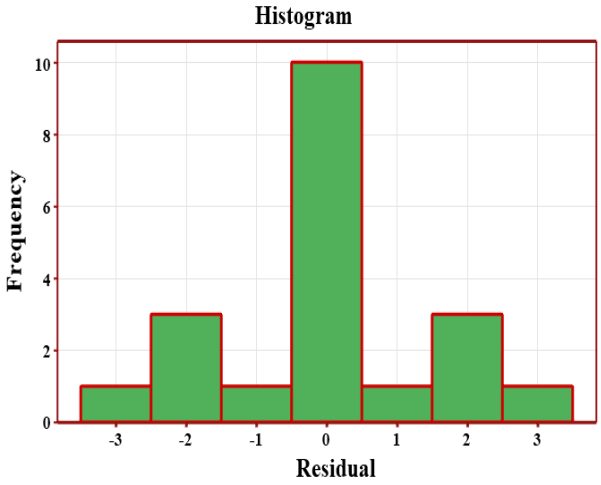

(b) Histogram

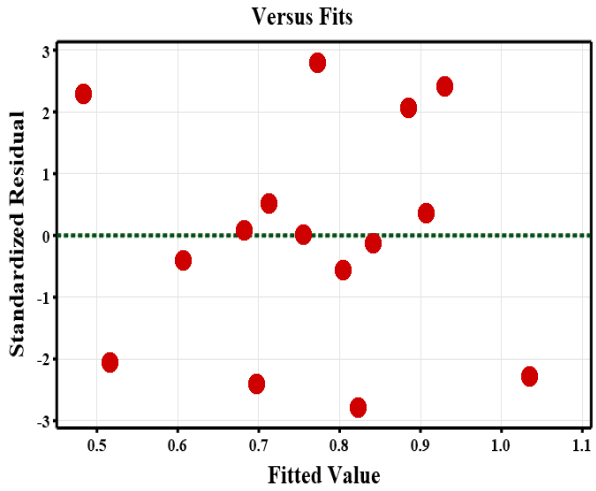

(c) Versus fits

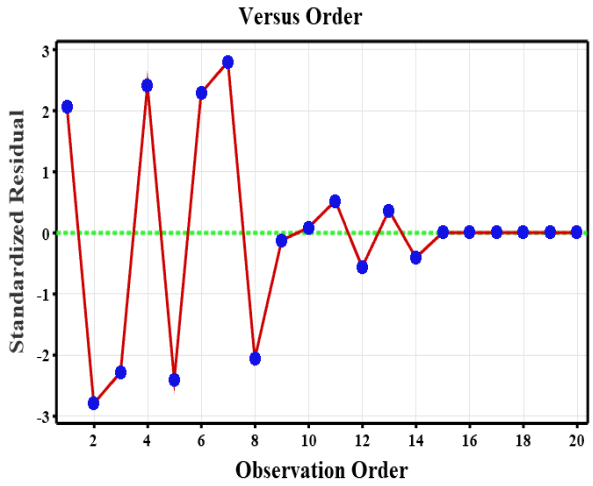

(d) Versus order

Figures 10. Residual plots for the Nusselt number.

6. Sensitivity analysis

The sensitivity analysis is a widely used technique in various scientific disciplines to examine how variations in input parameters influence outputs responses in a physical process. It is employed to evaluate the efficiency of responses within a system. In the present study, the sensitivity of the Nusselt number (Nu) with respect to the input factors A, B, and C is investigated. Using Eq (19), the sensitivity functions of the output response (Nu) can be expressed as

$$\frac{\partial Nu}{\partial A} = 0.01438\ \ A - 0.01070\ \ B - 0.03790\ \ C, \tag{20}$$

$$\frac{\partial Nu}{\partial B} = 0.04573 + 0.00746B \quad - 0.01070 \;\; A - 0.01847 \;\; C, \tag{21}$$

$$\frac{\partial Nu}{\partial C} = \quad 0.00404 \;\; C - 0.03790 \;\; A - 0.01847 \;\; B. \tag{22}$$

Table 7 presents the sensitivity of the response output Nu when maintaining input factor B at its medium level, i.e., B = 0, using Eqs (20)−(22). Bar charts illustrating the sensitivity of the response with respect to the input parameters are shown in Figures 11(a)–(c). An increase in the response is indicated when the bar extends in the positive direction, whereas a decrease is indicated by the bar extending in the negative direction. Greater bar height indicate higher sensitivity of the response to the input parameters.

In this analysis, the sensitivities of the output (Nu) to the input variables (λ_0, D_f, S_r) are computed for all levels (low, medium, and high). The sensitivity of Nu to parameter λ_0 is positive for all levels but slightly negative at $A = 1$ and $C = 1$. In contrast, negative sensitivities of Nu are observed for factors D_f and S_r. These results indicate that Nu is directly proportional to λ_0, meaning that the sensitivity of Nu increases as λ_0 increases. In contrast, the sensitivity of Nu decreases with increasing values of D_f and S_r. The response Nu is most sensitive to parameter λ_0 at $A = -1$ and $C = 1$, whereas Nu is most sensitive to factor D_f, as indicated by the greater height of the corresponding bar charts compared to those for λ_0 and S_r.

Table 7. Sensitivity of response output Nu when $B = 1.0$.

A	C	$\frac{\partial Nu}{\partial A}$	$\frac{\partial Nu}{\partial B}$	$\frac{\partial Nu}{\partial C}$
	0.3	0.022460	0.038605	-0.035400
0.5	0.6	0.041410	0.029370	-0.033380
	0.9	0.060360	0.020135	-0.031360
	0.3	-0.015270	0.033255	-0.054350
1.0	0.6	-0.034220	0.024020	-0.052330
	0.9	-0.053170	0.014785	-0.050310
	0.3	-0.008080	0.027905	-0.073300
1.5	0.6	-0.027030	0.018670	-0.071280
	0.9	-0.045980	0.009435	-0.069260

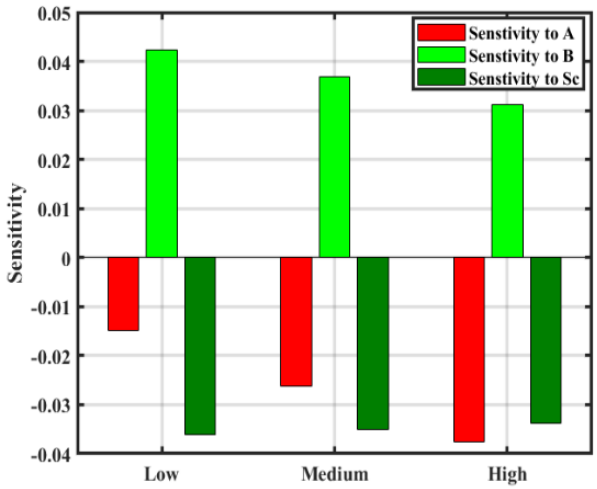

(a) When $A = -1$.

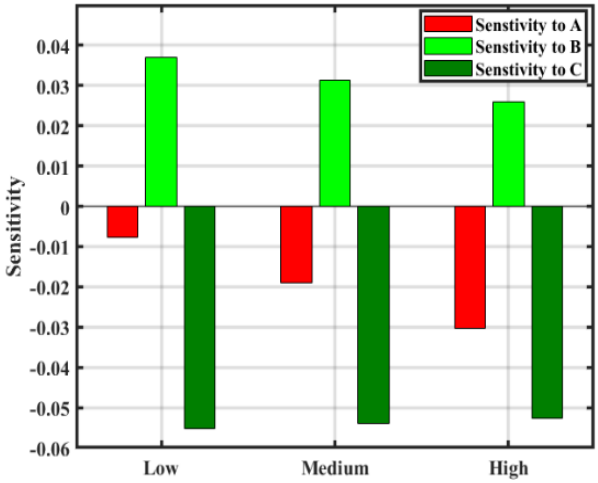

(b) When $A = 0$.

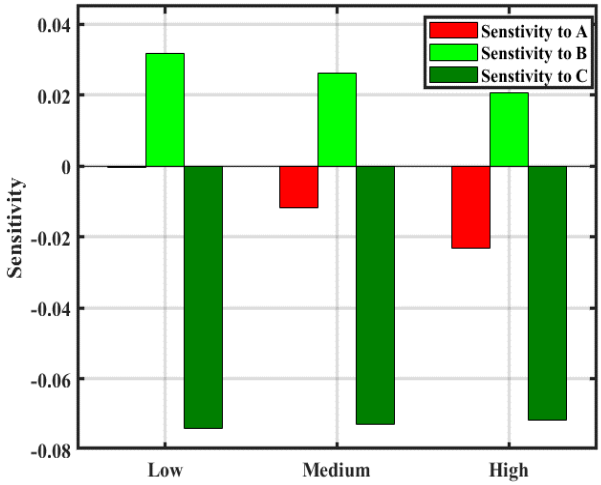

(c) When $A = 1$.

Figures 11. Sensitivity plots for output Nu by keeping $B = 0$.

7. Conclusions

We analyzed the boundary-layer flow of a third-grade Ellis fluid over a vertical stretching cylinder, incorporating the combined effects of Soret, Dufour, and chemical reaction. The nonlinear rheology model captures both shear-thinning behavior and higher-order stress effects beyond Newtonian behavior. Additionally, the cross-diffusion mechanisms highlight the strong coupling between thermal and solutal transport in multicomponent systems. The main findings are summarized as follows:

- Velocity increases with an increase in the Ellis fluid parameter. This parameter indicates that the effective viscosity of the fluid decreases under shear. As a result, higher values of the Ellis fluid parameter reduce flow resistance, leading to an increase in the velocity profile along the surface.
- The third-grade fluid parameter represents nonlinear elastic and viscous effects. As its value increases, the nonlinear shear-thinning behavior reduces resistance to motion, allowing fluid

layers to slide more easily. This enhances momentum transfer and increases velocity near the stretching surface.

- The Dufour effect induces heat transfer due to concentration gradients. As the Dufour parameter increases, enhanced thermal diffusion reduces concentration differences. Increasing the Dufour effect causes a reduction in concentration at the stretching surface.
- As the chemical reaction increases, the rate of reactant consumption increases, resulting in a decrease in the concentration profile.

In future work, we will evaluate if our model can be extended to curved stretching surfaces. Further improvements could consider the impacts of MHD, viscous dissipation, induced magnetic fields, and other mechanisms.

Author contributions

Nadeem Abbas: Conceptualization, methodology, formal analysis, writing–original draft; Wasfi Shatanawi: Supervision, validation, writing–review & editing. All authors have read and approved the final version of the manuscript for publication.

Use of Generative-AI tools declaration

The authors declare they have not used Artificial Intelligence (AI) tools in the creation of this article.

Acknowledgments

The authors would like to thank Prince Sultan University for their support through the TAS research lab.

Conflict of interest

A declaration of interest statement demonstrates that the authors have no financial, personal, or professional conflicts.

References

1. S. Matsuhisa, R. B. Bird, Analytical and numerical solutions for laminar flow of the non-Newtonian ellis fluid, *AIChE J.*, **11** (1965), 588–595. https://doi.org/10.1002/aic.690110407
2. Y. Li, B. Yu, J. Chen, C. Wang, Analysis of permeability for Ellis fluid flow in fractal porous media, *Chem. Eng. Commun.*, **195** (2008), 1240–1256. https://doi.org/10.1080/00986440801942018
3. V. O. Kheyfets, S. L. Kieweg, Gravity-driven thin film flow of an Ellis fluid, *J. Non-Newton. Fluid*, **202** (2013), 88–98. https://doi.org/10.1016/j.jnnfm.2013.09.010
4. N. Ali, S. Hussain, K. Ullah, O. A. Bég, Mathematical modelling of two-fluid electro-osmotic peristaltic pumping of an Ellis fluid in an axisymmetric tube, *Eur. Phys. J. Plus*, **134** (2019), 141. https://doi.org/10.1140/epjp/i2019-12488-2

5. A. Abbasi, S. U. Khan, W. Farooq, F. M. Mughal, M. I. Khan, B. C. Prasannakumara, et al., Peristaltic flow of chemically reactive Ellis fluid through an asymmetric channel: Heat and mass transfer analysis, *Ain Shams Eng. J.*, **14** (2023), 101832. https://doi.org/10.1016/j.asej.2022.101832
6. S. Shaheen, H. Huang, F. A. Al-Yarimi, M. B. Arain, Theoretical analysis of Ellis fluid flow in two layers due to metachronal propulsion subject to heat and mass transfer: Application in biological function, *Case Stud. Therm. Eng.*, **59** (2024) 104446. https://doi.org/10.1016/j.csite.2024.104446
7. A. Mishra, Analysis of radiative Ellis hybrid nanofluid flow over a stretching/shrinking cylinder embedded in a porous medium with slip condition, *Multiscale Multi. Mod.*, **8** (2025), 282. https://doi.org/10.1007/s41939-025-00871-7
8. S. Abdal, M. Ajmal, B. C. Prasannakumara, N. A. Shah, R. M. Zulqarnain, S. J. Yook, Significance of nanoparticles concentration for heat and mass transfer of Ellis fluid dynamics across a stretching wall, *J. Therm. Anal. Calorim.*, 2025, 1–13. https://doi.org/10.1007/s10973-025-14029-7
9. B. Sahoo, Hiemenz flow and heat transfer of a third grade fluid, *Commun. Nonlinear Sci.*, **14** (2009), 811–826. https://doi.org/10.1016/j.cnsns.2007.12.002
10. T. Hayat, A. Shafiq, A. Alsaedi, M. Awais, MHD axisymmetric flow of third grade fluid between stretching sheets with heat transfer, *Comput. Fluids*, **86** (2013), 103–108. https://doi.org/10.1016/j.compfluid.2013.07.003
11. T. Hayat, A. Shafiq, A. Alsaedi, MHD axisymmetric flow of third grade fluid by a stretching cylinder, *Alex. Eng. J.*, **54** (2015), 205–212. https://doi.org/10.1016/j.aej.2015.03.013
12. A. T. Akinshilo, Steady flow and heat transfer analysis of third grade fluid with porous medium and heat generation, *Eng. Sci. Technol.*, **20** (2017), 1602–1609. https://doi.org/10.1016/j.jestch.2017.11.012
13. S. Khan, M. M. Selim, A. Khan, A. Ullah, T. Abdeljawad, Ikramullah, et al., On the analysis of the non-Newtonian fluid flow past a stretching/shrinking permeable surface with heat and mass transfer, *Coatings*, **11** (2021), 566. https://doi.org/10.3390/coatings11050566
14. N. Fatima, M. Nazeer, M. M. Lashin, M. M. Ghafar, M. R. Gorji, M. K. Hameed, Developments of electro-osmotic two-phase flows of fourth-grade fluid through convergent and divergent channels, *Mathematics*, **11** (2023), 1832. https://doi.org/10.3390/math11081832
15. S. Saleem, J. Alzabut, Exact exploration of time fractional-based magnetized flow of a generalized second grade fluid through an oscillating rectangular duct, *Int. J. Geom. Methods M.*, 2024, 2440031.
16. X. Xin, I. Khan, A. M. Alqahtani, T. Chinyoka, R. Alroobaea, R. Zulkifli, et al. Numerical simulations of third-grade fluid flow with exothermic reactions in porous media-saturated vertical microchannels, *Numer. Heat Tr. B-Fund.*, **86** (2025), 2473–2493. https://doi.org/10.1080/10407790.2024.2345508
17. A. Abbas, A. Khan, T. Abdeljawad, N. Becheikh, L. Kolsi, Theoretical analysis of MHD Darcy-Forchheimer porous media for hybrid nanomaterial flow with third-grade fluid over an exponential stretching sheet, *Fractals*, 2025.
18. J. Kim, Y. T. Kang, C. K. Choi, Soret and Dufour effects on convective instabilities in binary nanofluids for absorption application, *Int. J. Refrig.*, **30** (2007), 323–328. https://doi.org/10.1016/j.ijrefrig.2006.04.005

19. M. B. K. Moorthy, K. Senthilvadivu, Soret and Dufour effects on natural convection flow past a vertical surface in a porous medium with variable viscosity, *J. Appl. Math.*, **2012** (2012), 634806. https://doi.org/10.1155/2012/634806
20. A. Majeed, T. Javed, A. Ghaffari, Numerical investigation on flow of second grade fluid due to stretching cylinder with Soret and Dufour effects, *J. Mol. Liq.*, **221** (2016), 878–884. https://doi.org/10.1016/j.molliq.2016.06.065
21. M. Y. Malik, O. D. Makinde, Parabolic curve fitting study subject to Joule heating in MHD thermally stratified mixed convection stagnation point flow of Eyring-Powell fluid induced by an inclined cylindrical surface, *J. King Saud Univ. Sci.*, **30** (2018), 440–449. https://doi.org/10.1016/j.jksus.2017.02.003
22. A. Shojaei, A. J. Amiri, S. S. Ardahaie, K. Hosseinzadeh, D. D. Ganji, Hydrothermal analysis of Non-Newtonian second grade fluid flow on radiative stretching cylinder with Soret and Dufour effects, *Case Stud. Therm. Eng.*, **13** (2019), 100384. https://doi.org/10.1016/j.csite.2018.100384
23. A. A. Khan, N. Abbas, S. Nadeem, Q. H. Shi, M. Y. Malik, M. Ashraf, et al., Non-Newtonian based micropolar fluid flow over nonlinear starching cylinder under Soret and Dufour numbers effects, *Int. Commun. Heat Mass*, **127** (2021), 105571. https://doi.org/10.1016/j.icheatmasstransfer.2021.105571
24. P. Kumar, R. S. Yadav, O. D. Makinde, Numerical study of Williamson fluid flow and heat transfer over a permeable stretching cylinder with the effects of Joule heating and heat generation/absorption, *Heat Transfer*, **52** (2023), 3372–3388. https://doi.org/10.1002/htj.22832
25. H. Basha, Magnetized dissipative Soret and Dufour effects on thermally radiative Casson fluid flow over a stretching cylinder with Cattaneo–Christov heat and mass flux models, *Wave. Random Complex*, 2023, 1–29. https://doi.org/10.1080/17455030.2023.2206491
26. G. Dharmaiah, S. Dinarvand, J. R. Prasad, S. Noeiaghdam, M. Abdollahzadeh, Non-homogeneous two-component buongiorno model for nanofluid flow toward Howarth's wavy cylinder with activation energy, *Results Eng.*, **17** (2023), 100879. https://doi.org/10.1016/j.rineng.2023.100879
27. P. Thiyagarajan, S. Sathiamoorthy, H. Balasundaram, O. D. Makinde, U. F. Gamiz, S. Noeiaghdam, et al., Mass transfer effects on mucus fluid in the presence of chemical reaction, *Alex. Eng. J.*, **62** (2023), 193–210. https://doi.org/10.1016/j.aej.2022.06.030
28. E. N. Thabet, A. M. A. Alla, H. A. Hosham, S. M. M. El-Kabeir, Entropy generation in peristaltic transport of bio-convective couple stress blood nanofluid with chemotactic microorganisms involving viscous dissipation and slip effects, *Alex. Eng. J.*, **102** (2024), 361–380. https://doi.org/10.1016/j.aej.2024.05.062
29. A. M. Abd-Alla, E. N. Thabet, H. A. Hosham, S. M. M. El-Kabeir, Significance of variable thermal conductivity and suction/injection in unsteady MHD mixed convection flow of Casson Williamson nanofluid through heat and mass transport with gyrotactic microorganisms, *ZAMM-J. Appl. Math. Mech.*, **104** (2024), e202300501. https://doi.org/10.1002/zamm.202300501
30. M. Ali, N. Abbas, W. Shatanawi, Soret and Dufour effects on Sutterbynanofluid flow over a Riga stretching surface with variable thermal conductivity, *Mod. Phys. Lett. B*, **39** (2025), 2450455. https://doi.org/10.1142/S0217984924504554
31. B. Ahmed, F. Akbar, A. Ghaffari, S. U. Khan, M. I. Khan, Y. D. Reddy, Soret and Dufour aspects of the third-grade fluid due to the stretching cylinder with the Keller box approach, *Wave. Random Complex*, **35** (2025), 7236–7248. https://doi.org/10.1080/17455030.2022.2085891

32. K. Bhattacharyya, Boundary layer flow and heat transfer over a permeable shrinking cylinder with mass suction, *Int. J. Appl. Mech. Eng.*, **18** (2013). https://doi.org/10.2478/ijame-2013-0062
33. G. K. Ramesh, S. Manjunatha, G. S. Roopa, A. J. Chamkha, Hybrid (ND-Co_3O_4/EG) nanoliquid through a permeable cylinder under homogeneous-heterogeneous reactions and slip effects, *J. Therm. Anal. Calorim.*, **146** (2021). https://doi.org/10.1007/s10973-020-10106-1

AIMS Press